Chemical Engineering Journal 421 (2021) 129767

Contents lists available at ScienceDirect

Chemical Engineering Journal

journal homepage: www.elsevier.com/locate/cej

Electrochemical synthesis of binder-free interconnected nanosheets of Mn-doped Co_3O_4 on Ni foam for high-performance electrochemical energy storage application

N.C. Maile [a], Mokrema Moztahida [a], Ahsan Abdul Ghani [a], Muzammil Hussain [a], Khurram Tahir [a], Bolam Kim [a], S.K. Shinde [b], V.J. Fulari [c], Dae Sung Lee [a,*]

[a] Department of Environmental Engineering, Kyungpook National University, 80 Daehak-ro, Buk-gu, Daegu 41566, Republic of Korea
[b] Department of Biological and Environmental Science, College of Life Science and Biotechnology, Dongguk University, 32 Dongguk-ro, Biomedical Campus, Ilsandong-gu, Siksa-dong, 10326 Goyang-si, Gyeonggi-do, Republic of Korea
[c] Holography and Materials Research Laboratory, Department of Physics, Shivaji University, Kolhapur 416004, M.S., India

ARTICLE INFO

Keywords:
Mn-doped Co_3O_4
Potentiodynamic deposition
Nanosheet
Supercapacitor
Electrochemical energy storage

ABSTRACT

In this study, various nanostructures of Mn-doped Co_3O_4 were synthesized on Ni foam using binder-free electrochemical technology for electrochemical energy storage applications. Using the cyclic voltammetry method with different scan rates, diverse nanostructures, i.e., irregularly oriented nanooctahedra, interconnected standing nanosheets, and nanopetals of Mn-doped Co_3O_4, were obtained. The standing interconnected nanosheets on the Ni foam exhibited remarkable supercapacitive performance due to the void space between the sheets and mesoporous structure, which provided additional active sites for faradic transitions. The nanosheets exhibited excellent electrochemical performance with a maximum specific capacitance of 1005F g^{-1} and a cyclic stability of 88% during 5000 charge–discharge cycles. Moreover, an asymmetric supercapacitor was assembled comprising activated carbon on Ni foam and interconnected nanosheets of Mn-doped Co_3O_4 on Ni foam as negative and positive electrodes, respectively. This assembled device exhibited an improved potential of 1.6 V, a maximum specific energy of 20.6 Wh kg^{-1}, and a maximum specific power of 16 kW kg^{-1} with 80.6% capacity retention after 2000 charge–discharge cycles, which is superior for SC devices.

1. Introduction

Effective electric energy storage and retrieval are important aspects for the development of sustainable and renewable energy devices. Most of the research on this topic has focused on the use of nontoxic, abundantly available materials for low production cost and enhanced operational safety [1]. In particular, Li-ion battery technology stands out for its ability to deliver high specific energy in various electrical appliances, including medical devices and communication implements [2,3]. However, for the development of next-generation hybrid devices, supercapacitors (SCs) with high specific power that can provide large amounts of electrical energy in short periods are required. Basic electrochemical reactions occurring at the electrodes of SCs play a vital role in SC operation. In this context, SCs can be divided into two types: electrical double-layer capacitors (EDLC) with nonfaradic charge storage and pseudocapacitors with faradic charge storage. In general, SCs based on carbon nanomaterials such as carbon nanotubes, graphene oxides, and activated carbon (AC) are EDLCs, which exhibit high electrical conductivity and large surface areas. In contrast, transition metal oxides (TMOs), including MnO_2, Mn_2O_3, RuO_2, Co_3O_4, Fe_2O_3, and TiO_2, which undergo reversible faradic reactions, are used as pseudocapacitive materials [1,4]. These TMOs can deliver much higher energy density than carbon-based materials [1,2]. In particular, thin-film nanostructures of Co_3O_4 are considered to be good pseudocapacitive materials offering broad redox peaks over wider potential ranges compared with the sharp redox peaks of battery electrode materials [5,6].

Unfortunately, the low conductivity of TMO materials is a limitation for SC applications, and extensive research efforts have been devoted to enhance their performance. Studies have shown that TMOs having more than one cation exhibit better performance than oxides with single cations [7-9] and that the properties of core TMOs can be altered by

* Corresponding author.
E-mail address: daesung@knu.ac.kr (D.S. Lee).

https://doi.org/10.1016/j.cej.2021.129767
Received 21 January 2021; Received in revised form 29 March 2021; Accepted 7 April 2021
Available online 16 April 2021

doping with different cations [7,8,10]. In selective studies, Fe and Mn doping lowers the bandgap energy of Co_3O_4, and Fe doping induces a slight ferromagnetic behavior in Co_3O_4 [8,10] and affords excellent catalytic activity toward oxygen reduction reactions (ORR) and oxygen evolution reactions (OER) [11-13]. Meanwhile, La doping in Co_3O_4 has been shown to improve the photocatalytic activity [7] and selective sensitivity toward iodine, hydroxylamine, and sulfite [14-16]. In addition, the OER and ORR electrocatalytic activity of Co_3O_4 are enhanced by Ni doping and catalytic propane oxidation [13,17-19]. Cu-doped Co_3O_4 exhibits greatly enhanced catalytic activity toward fluorine oxidation [20], and Fe/Cr-doped Co_3O_4 shows enhanced catalytic activity toward CO oxidation at low temperatures [21]. Cr-doped Co_3O_4 hierarchical nanostructures show excellent response toward xylene as a selective gas sensor [22], and Mo-doped Co_3O_4 nanoparticles have excellent activity toward OER [23]. Pd-doped Co_3O_4 nanowire arrays are excellent H_2O_2 electroreduction catalysts [24]. Cd doping in Co_3O_4 nanosheets improves the electroactive properties toward electrochemical energy storage [25]. Zn-doped Co_3O_4 shows excellent electrochemical properties toward nonenzymatic glucose detection [26]. Mn doping in Co_3O_4 promotes the selective catalytic reduction of NO with NH_3 [27], improves the intrinsic conductivity [28], enhances the activity and stability of low-temperature catalytic CO oxidation [29], and affords excellent OER electrocatalytic properties [30]. Furthermore, Mn-doped Co_3O_4 has been studied for energy storage applications because Mn provides extra active sites for charge conversion [31-34].

Electrochemical synthesis can produce binder-free nanostructures directly on conductive surfaces; this reduces the intrinsic resistance of active electrode materials [35-40]. The type of electrochemical synthesis depends on the mode of deposition. Jagadale et al. studied the nanostructured formation of Co_3O_4 using galvanostatic, potentiostatic, and potentiodynamic electrochemical approaches. In the galvanostatic mode, the flow of charges at the subject electrode is maintained, whereas, in the potentiostatic mode, the potential of charges at the subject electrode is maintained. In both modes, the desired growth of nanostructures can be achieved by tuning the deposition time. The reaction involves initial nucleation, hemispherical mass transfer, and subsequent diffusion-controlled linear mass transfer to develop different nanostructures [6,41]. However, in the potentiodynamic measurement, which is generally known as cyclic voltammetry (CV), the potential of the subject electrode varies between two fixed potentials with different cycling rates, and the growth of nanostructures depends on the number of cycles and the cycling rate [6]. For the development of Mn-doped Co_3O_4 nanostructures for SC application, the use of a simple CV technique would be useful and cost-effective, particularly for applications requiring binder-free nanostructures.

In this study, Mn-doped Co_3O_4 nanostructures were grown on Ni foam as a substrate using a CV method at different scan rates, which was carefully studied and confirmed by different characterization methods. Electrochemical properties were investigated for electrochemical energy storage application. The CV, galvanostatic charge–discharge (GCD) method along with electrochemical impedance spectroscopy (EIS) studies exhibited very good insights into the energy storage properties of the synthesized Mn-doped Co_3O_4 nanostructures, which eventually helped to understand the correlation between nanostructured materials and electrical energy storage properties. In addition, the constructed asymmetric aqueous assembly of SC explored the practical and useful aspect of Mn-doped Co_3O_4 nanostructures.

2. Materials and methods

2.1. Chemicals

All the chemicals used for the study were analytical grade, so used without any further purification. Manganese(II)chloride tetrahydrate [$MnCl_2{\cdot}4H_2O$] was purchased from Hayashi pure chemical Ind. Ltd. (Japan). Cobalt(II)chloride hexahydrate [$CoCl_2{\cdot}6H_2O$] was purchased from Samchun chemicals (Republic of Korea). Potassium hydroxide [KOH] was purchased from Daejung Chemicals (Republic of Korea).

2.2. Preparation of Mn-doped Co_3O_4 electrode

For electrode fabrication, battery-grade Ni foam (1 cm × 1 cm × 0.8 mm) was used as a current collection substrate owing to its three-dimensional (3D) microporous structure and remarkable conductivity [37,42,43]. These substrates were rinsed carefully with 3 M HCl, deionized (DI) water, and ethanol via ultrasonication. A precursor bath containing 0.1 M $MnCl_2$ and 0.064 M $CoCl_2$ in DI water was prepared at room temperature. As shown in the schematic depicted in Fig. 1, in the three electrode setup, the cleaned Ni foam, graphite, and Ag/AgCl electrode were submerged into the bath to serve as working, counter, and reference electrodes, respectively. During CV electrodeposition, the potential (E) of the Ni foam varied between − 1.0 and 0.0 V against the Ag/AgCl electrode with scan rates (ν) of 30, 50, and 100 mV s^{-1}. The applied potential profiles of these ν values are depicted in the inset of Fig. 1. Subsequently, Ni foams with electrodeposited material were cleaned in DI water, dried at room temperature, and subjected to calcination in a furnace at 673 K for 2 h. The electrodes prepared at ν values of 30, 50, and 100 mV s^{-1} were labeled as samples S-30, S-50, and S-100, respectively.

The activated carbon (AC) electrode was fabricated by mixing AC, carbon black and PVDF with the mass ratio of 80:10:10 in 1-Methyl-2-pyrrolidinone solvent to obtain a slurry, and followed by coating the slurry onto nickel foam and drying the supported nickel foam at 80 °C for 12 h under vacuum. Then the aqueous asymmetric SC device was assembled using S-50 as a positive electrode (cathode) and the activated carbon (AC) as a negative electrode (anode) in 2 M KOH. Moreover, the SC device was subjected to CV, GCD, and cyclic stability studies.

2.3. Characterization of material

Prepared samples were subjected to X-ray diffraction (XRD, Panalytical (EMPYREAN) with Cu Kα −1.54 Å) analysis, field emission scanning electron microscope-energy dispersive X-ray spectroscopy analysis (FESEM-EDS system, HITACHI SU8220, Japan), Raman spectroscopy (Renishaw inViareflex spectrometer, Gloucestershire, UK with Laser line of 532 nm) and X-Ray Photoelectron Spectroscopy (XPS, ThermoFisher -NEXSA, USA).

2.4. Electrochemical measurement

Three electrode arrangement was used for mono electrode testing in 2 M KOH electrolyte. As prepared Mn-doped Co_3O_4 on Ni foam was connected to test working terminal, platinum plate was connected to counter and Ag/AgCl was connected to reference terminal of workstation, respectively. All the necessary electrochemical analysis were performed using WizEIS l200Premium workstation (Wiz MAC, Republic of Korea).

3. Result and discussion

3.1. Formation of Mn-Doped Co_3O_4

In CV, the potential of the working electrode varies between the potential limits with respect to the reference electrode. These potential limits can be scanned rapidly or slowly by tuning the ν to high or low values [44]. As shown in the inset in Fig. 1, a ν of 30 mV s^{-1} required a long time to complete the CV cycle. Here, the CV was performed between − 1.0 and 0 V at ν values of 30, 50, and 100 mV s^{-1}. The first CV curve, recorded at 50 mV s^{-1}, is shown in Fig. S1(a). During the negative scan from 0 to − 1.0 V, a sharp decrease in current density (j) was initially observed up to − 0.19 V, followed by a plateau from − 0.19 to − 0.57 V. In this underpotential condition, codeposition of Mn and Co

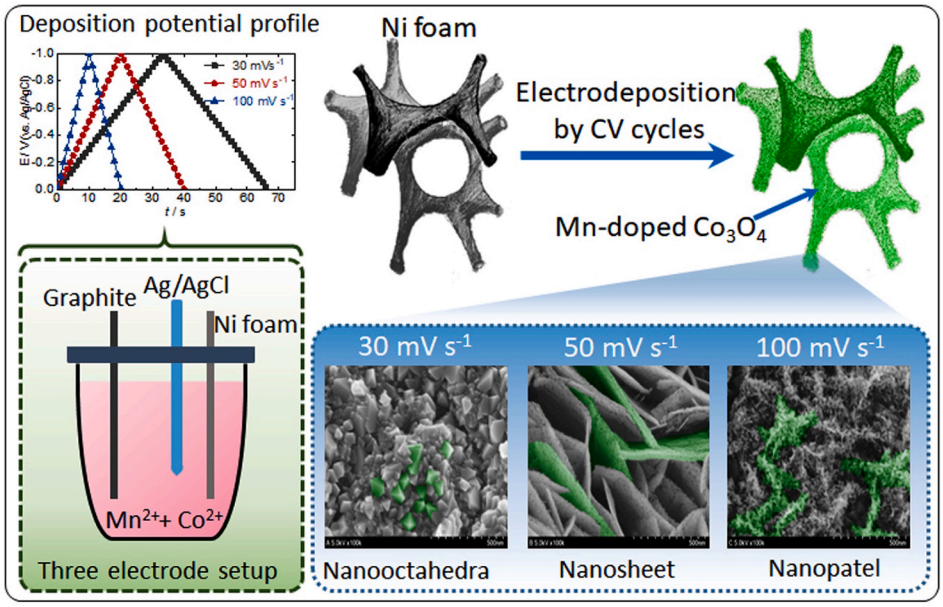

Fig. 1. Schematic illustration of the electrodeposition process for the Mn-doped Co_3O_4 nanostructures on Ni foam substrate.

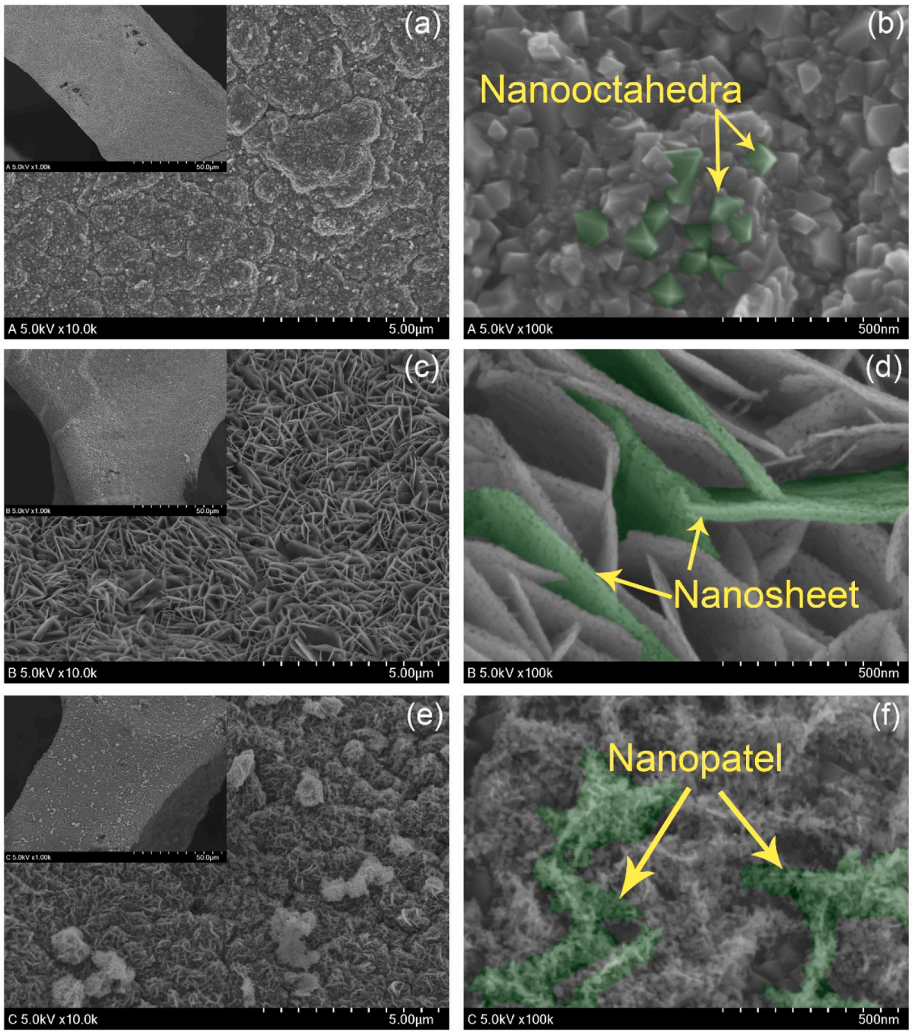

Fig. 2. FESEM images of Mn-doped Co_3O_4 prepared at scan rates of 30 mV s^{-1} (a–b) [S-30], 50 mV s^{-1} (c–d) [S-50], and 100 mV s^{-1} (e–f) [S-100].

occurred to form a monolayer. However, *j* greatly decreased from − 0.57 to − 1.0 V, with a broad reduction peak at − 0.81 V. At this potential region, 3D nucleation and growth of the material was initiated by the deposition of metals (M = Mn, Co) according to Eq. (1):

$$M^{2+}_{(aq)} + 2OH^{-}_{(aq)} \rightarrow M(OH)_{2(s)} \quad (1)$$

Besides, in the overpotential region at −1.0 V, the massive reduction of water generates more hydroxyl ions lead to the massive growth of material [40,45].

In the reverse scan, *j* was notably lower till − 0.57 V, followed by a plateau up to − 0.47 V with partial broad oxidation peaks. The cathodic crossover at − 0.57 V corresponds to the nucleation overpotential, which confirms the nucleation and growth of the material [45]. Furthermore, as the CV cycle progressed, the peak *j* of the CV became more negative. As shown in Fig. S1(b), the peak *j* of the 50th CV cycle was more negative than that of the 1st CV cycle, which suggests an increase in electronic conductivity of the overall electrode that ensuring the growth of material on the Ni foam with CV cycling. Subsequent calcination of the material resulted in the formation of Mn-doped Co_3O_4 on the Ni foam according to Eq. (2):

$$M(OH)_{2(s)} \rightarrow Mn_xCo_{3-x}O_{4(s)} \quad (2)$$

The different ν of CV deposition can greatly affect the growth of the material. In the three-electrode system, a high scan rate applied to the working electrode can rapidly change its potential, which affects the electrochemical reactivity on its surface. Rapid changes in the potential provide less time for the cations to react and settle on the Ni foam, according to Eq. (1). Therefore, in a single CV cycle, the amount of material deposited on the Ni foam is higher at 30 mV s^{-1} than at 100 mV s^{-1}. Here, for comparison, the same deposition masses were achieved in S-30, S-50, and S-100 by running 30, 50, and 100 CV cycles at ν values of 30, 50, and 100 mV s^{-1}, respectively [45]. After calcination, the deposited mass of Mn-doped Co_3O_4 on Ni foam was estimated as ~ 2 mg cm^{-2}.

3.2. FESEM study

Fig. 2 shows FESEM images of the Mn-doped Co_3O_4 nanostructures recorded at ν values of 30, 50, and 100 mV s^{-1}. At the low ν, the cations from the solution had more time to react continuously with the hydroxyl ions at the overpotential region of each CV cycle, resulting in continuous nucleation and material growth. At the ν of 30 mV s^{-1}, the slow and continuous growth of the material led to the formation of nonoverlapping micrometer-sized granules with distinct grain boundaries, as shown in the FESEM image of S-30 (Fig. 2(a)). The high-magnification image of this granular region shown in Fig. 2(b) reveals the presence of distinct nanooctahedra like nanostructures with irregular orientation. These shapes have their base formed on the grain surface, grown and pointed in the normal direction away from the base. An increase in the ν value to 50 mV s^{-1} decreased the time for nucleation and growth. As a result, interconnected nanosheets formed on the surface of S-50, as shown in Fig. 2(c). In this case, during initial cycling, the nucleation sites for nanosheets may be formed on the Ni surface. As cations had insufficient time to diffuse into the structure, with each cycle nanosheets grows at these nucleation sites. The high-resolution image of S-50 shown in Fig. 2 (d) reveals vertically aligned, distinct mesoporous nanosheets that are irregularly oriented and interconnected. At a higher ν of 100 mV s^{-1}, the nucleation time on the Ni surface was very short, which caused the formation of irregular structures in S-100. As shown in Fig. 2(e), the Ni surface was composed of irregular, distinct grains comprising connected clusters of chains. However, the high-resolution image as shown in Fig. 2 (f) clearly reveals the formation of petals clustered together in single branches connected to form a chain-like structure. This occurred because the cations had insufficient resting time to grow on the Ni surface [45]. The Mn-doped Co_3O_4 deposited at 30 mV s^{-1} exhibited a compact nanostructure surface, whereas a rough nanostructure surface with a less porous morphology formed at 100 mV s^{-1}. However, at 50 mV s^{-1}, a mesoporous structure was generated, which can improve the electrolyte ion diffusion. Uniform deposition of Mn-doped Co_3O_4 on the Ni foam can be clearly observed in the inset of FESEM image Fig. 2(a), (c), and (e).

3.3. XRD, Raman, XPS and EDS study

Recorded XRD profile of S-30, S-50 and S-100 shows highly intense peaks at 2θ angle of 44.48°, 51.82° and 76.37° which are ascribed to (1 1 1), (2 0 0) and (2 2 0) planes of Ni foam (JCPDS- 87–0712) as shown in Fig. 3(a) [46]. The remaining peaks are attributable to the cubic phase of Co_3O_4 (JCPDS-71–0816) [7,47]. Doping of Mn species into the spinel lattice of Co_3O_4 produced a small shift toward a lower 2θ diffraction angle in the peak position of the (3 1 1) plane [9]. Lattice parameter was calculated using Braggs relation for the cubic system, $d_{(hkl)} = a/\sqrt{(h^2 + k^2 + l^2)}$ for (3 1 1) plane and it is estimated as ~ 8.09 Å which is higher than reported for Co_3O_4, as a result of Mn doping [8-10]. The well-defined peaks observed in the XRD profile are indicative of the crystalline nature of Mn-doped Co_3O_4 [48]. Furthermore, in the Raman spectra of S-50 shown in Fig. 3(b), all the peaks that appear in the range 900–150 cm^{-1} are associated with the A_{1g}, E_g, and 3 F_{2g} activated Raman modes of the Co_3O_4 cubic spinel structure [49]. The Characteristic peak present at 194 cm^{-1} represents tetrahedral coordination of Co with O and the characteristic peak present at 691 cm^{-1} represents octahedral coordination of Co with O [50]. Doping of Mn did not produce any broadening of octahedral peak indicated spinel lattice structure is intact during the doping of Mn in Co_3O_4 lattice [51,52]. In addition, the XPS of S-50 revealed the presence of Mn, Co, O, and C elements (Fig. S2(a)) [53]. As shown in Fig. 3(c), the high-resolution XPS spectrum of the Mn 2p signal exhibits two broad peaks centered at binding energies of 642.8 and 653.7 eV corresponding to Mn $2p_{3/2}$ and Mn $2p_{1/2}$ spin orbits, respectively. However, the deconvolution of this spectrum shows binding energy peaks at 654.8 and 644.7 eV for Mn^{3+} ions, 653.4 and 642.0 eV for Mn^{2+} ions [53]. Similarly, as shown in Fig. 3(d), the high-resolution XPS spectrum of the Co 2p signal exhibits two broad peaks centered at binding energies of 780.1 and 795.3 eV, which are associated with Co $2p_{3/2}$ and Co $2p_{1/2}$ spin orbits, respectively. Meanwhile, the deconvoluted spectrum shows the binding energy peaks of Co^{3+} ions at 780.1 and 794.9 eV and those of Co^{2+} ions at 781.5 and 796.4 eV [53]. Moreover, as shown in Fig. 3(e), the deconvolution of the O 1s spin orbit affords three peaks at binding energies of 530.0, 531.1, and 533.4 eV, which can be ascribed to oxygen from metal–oxygen bonds from the lattice, surface oxygen ions, and hydroxyl oxygen stemming from water adsorbed onto the surface [45,53,54].

Moreover, the FESEM image of Mn-doped Co_3O_4 nanosheets is shown in Fig. 3(f) and respective EDS spectrum is shown in Fig. S2(b). EDS spectrum has signal associated with the Mn, Co and O element with ~ 1% of Mn doping. Elemental mapping image of nanosheets shows the uniform distribution of the Mn (Fig. 3(g)), Co(Fig. 3(h)) and O(Fig. 3(i)) elements confirming the formation of Mn-doped Co_3O_4 nanosheets on Ni foam. The presence of Ni and C from EDS and XPS analysis resulted from Ni-foam and the conducting paste tape that was used to fix samples [28].

3.4. Electrochemical study

The obtained nanostructured Mn-doped Co_3O_4 samples on the Ni foam with different morphologies were used directly as binder-free sample electrodes with no further treatment. The CV of Ni foam, S-30, S-50 and S-100 was performed between 0 and 0.75 V, obtained CV curves at ν of 60 mV s^{-1} is shown in Fig. 4(a). The Ni foam exhibited very low *j* with a weak redox signal due to the surface passivation of Ni in KOH [55,56]. Whereas, samples showed strong redox peaks associated with faradic reactions involving the conversion of Co^{2+}/Co^{3+}/

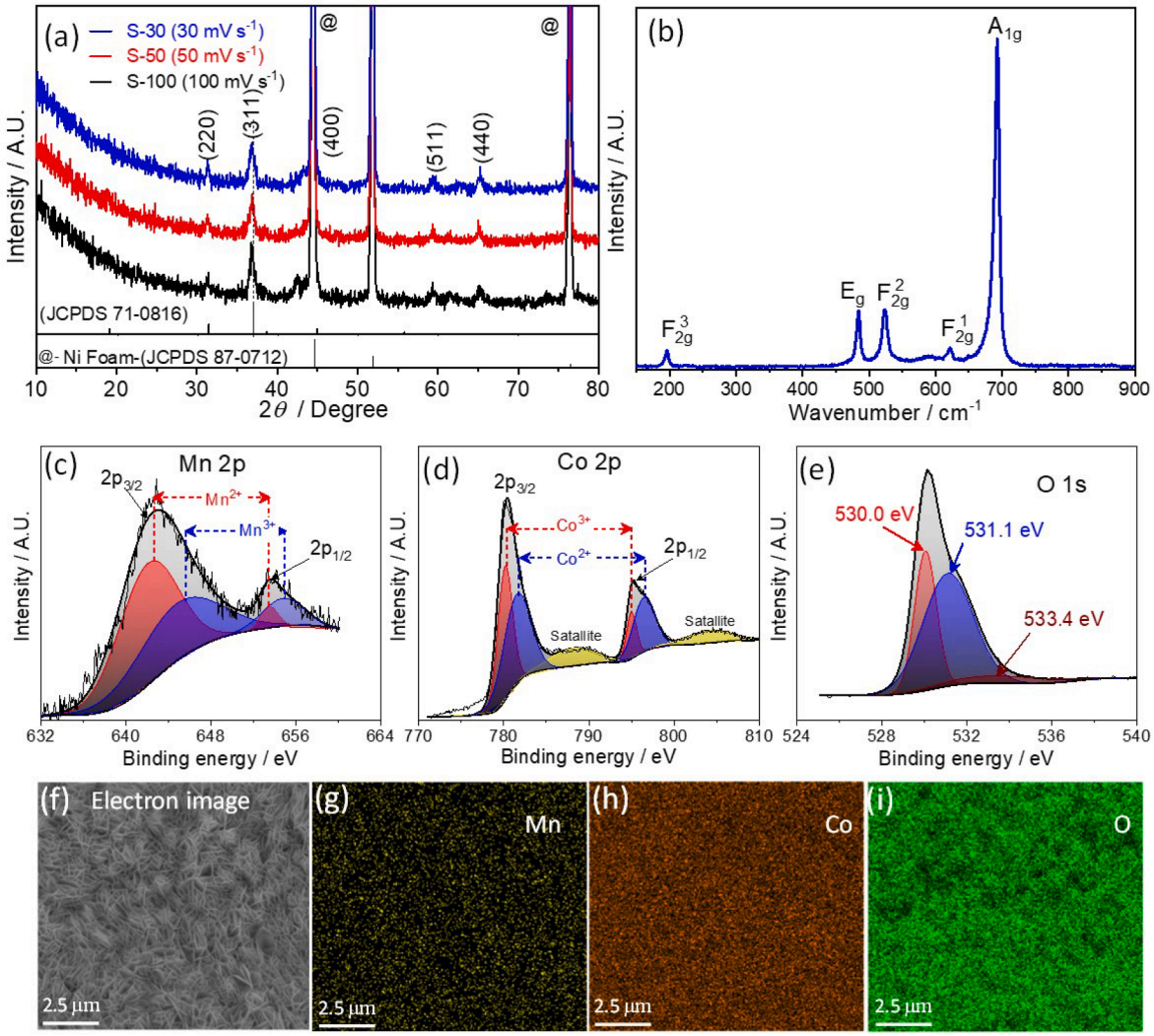

Fig. 3. (a) XRD profiles of Mn-doped Co_3O_4 deposited at scan rates of 30 (S-30), 50 (S-50), and 100 mV s^{-1} (S-100). (b) Raman spectra of S-50. High-resolution XPS of S-50 associated with Mn 2p(c), Co 2p(d), and O1 s(e) orbitals. FESEM image of (f) S-50 and the corresponding EDS mapping for (g) Mn, (h) Co, and (i) O elements.

Co^{4+}[57,58]. The broadness of redox peaks highlights surface diffusion process at Mn-doped Co_3O_4 nanostructures as a result of the following faradic reactions during the charge transfer process [40,59-61].

$$Mn_xCo_{3-x}O_4 + H_2O + OH^- \rightarrow xMnOOH + (3\text{-}x)CoOOH + xe^- \quad (3)$$

$$MnOOH + OH^- \leftrightarrow MnO_2 + H_2O + e^- \quad (4)$$

$$CoOOH + OH^- \leftrightarrow CoO_2 + H_2O + e^- \quad (5)$$

The S-50 sample exhibited the largest CV area, which can be ascribed to its mesoporous nanosheet-like morphology. The nanosheets provide a more accessible surface for the faradic transitions, thereby enhancing the overall electrochemical performance. In contrast, S-30 and S-100 exhibited smaller CV areas due to their compact and rough morphology. CV curves of S-50 at υ values of 5, 10, 20, 40, 60, 80, and 100 mV s^{-1} are shown in Fig. 4(b). The shapes of the CV curves were maintained; however, the shift in redox peaks with increasing ν suggests the occurrence of fast faradic transitions at the pores of the nanosheets [62]. The S-30 and S-100 samples exhibited similar CV behavior (Figs. S3(a), (b)). The inset in Fig. 4(b) shows the plots associated with anodic and cathodic peak j versus different ν [A] and $\nu^{1/2}$ [B]. The linearity observed in the plot of j versus $\nu^{1/2}$ indicates that most of the current generated was homogeneous, with diffusion-controlled charge transfer reactions occurring in the Mn-doped Co_3O_4 nanosheets with good electrochemical reversibility [63]. Two processes are generally involved in charge storage resulting in current generation (j(V)): capacitive storage led by surface reactions generating surface currents ($j_{cap}(V) = k_1\nu$), and charge storage due to the intercalation process generating diffusion-controlled currents ($j_{diff}(V) = k_2\nu^{1/2}$). Both currents are related by the expression $j(V) = j_{cap}(V) + j_{diff}(V) = k_1\nu + k_2\nu^{1/2}$, where k_1 and k_2 are constants [41,64]. Fig. 4(c) shows the estimated contribution of j_{cap}(V) in the total j(V) at $\nu = 5$ mV s^{-1}. Low capacitive currents in the redox peak region during charging (anodic scan) and discharging (cathodic scan) indicate that most of the generated current was caused by the intercalation of ions into the nanosheets. The inset in Fig. 4(c) shows a plot of the capacitive contribution at different ν values. The capacitive contribution owing to j_{cap}(V) increased with ν as a consequence of the less time available for the electrolyte ions to settle onto the nanostructured surface for intercalation at a given potential [45,65].

The GCD curves of S-30, S-50, and S-100 at $j = 1$ A g^{-1} are shown in Fig. 4(d). All the GCD curves exhibited similar, nonlinear charging and discharging behavior, demonstrating the reversible faradic charge conversion of Mn-doped Co_3O_4. During the charging process, the formation of the surface electric double layer at the electrode electrolyte interface caused a rapid increase in the potential. Subsequently, the electrode potential increased gradually as reversible faradic reactions occurred through the diffusion of ions at the nanostructured surface. During the discharging process, similar reactions occurred [1,41]. The S-50 showed

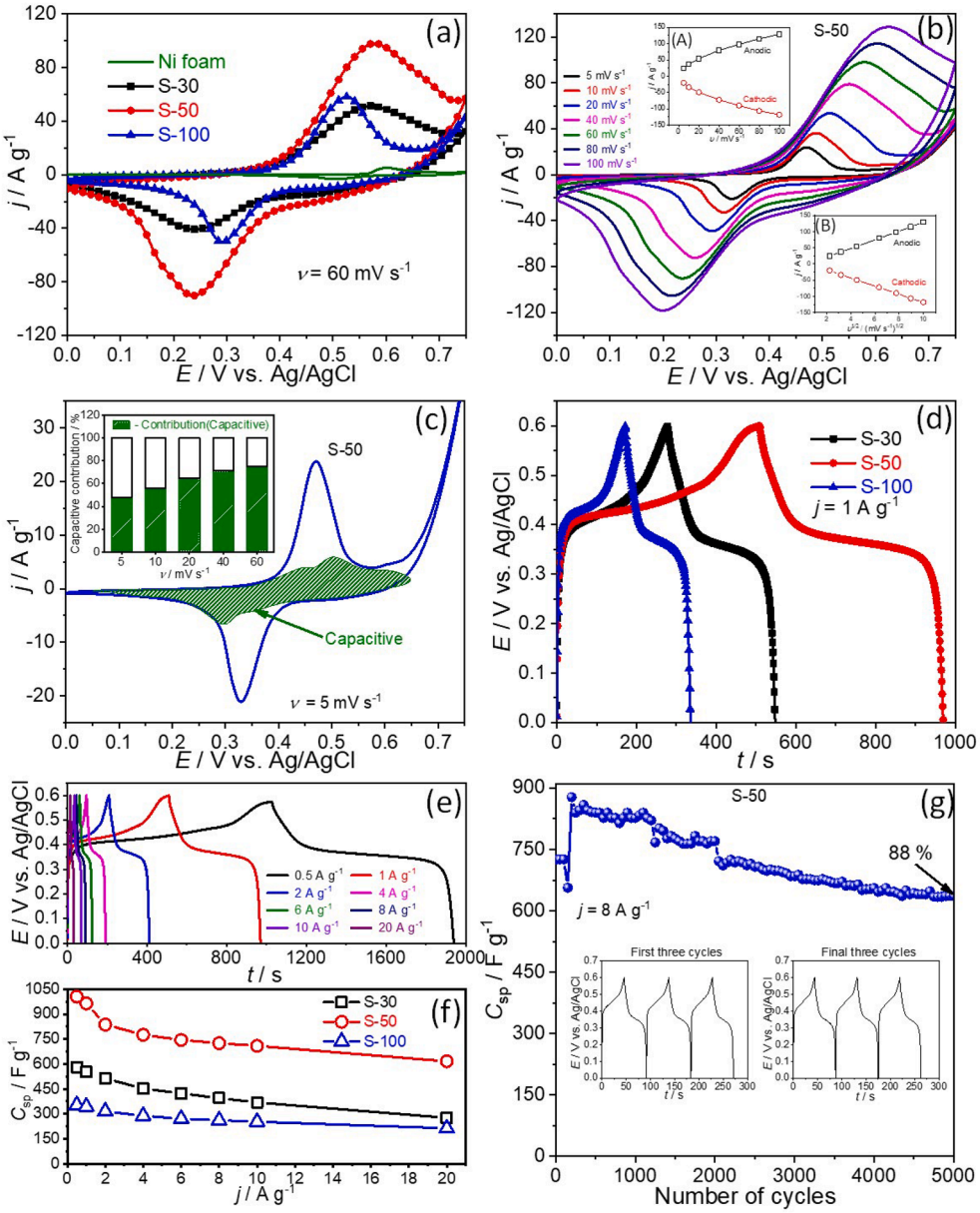

Fig. 4. (a) CV profiles of Ni foam, S-30, S-50, and S-100 at scan rate (ν) of 60 mV s^{-1} in 2 M KOH. (b) CV profiles of S-50 at ν values of 5, 10, 20, 40, 60, 80, and 100 mV s^{-1} (Inset: [A] plot of anodic and cathodic peak current density (j) versus ν; [B] plot of anodic and cathodic peak j versus $\nu^{1/2}$). (c) Experimental CV profile and calculated capacitive current (j_{cap}) profile of S-50 at $\nu = 5$ mV s^{-1}. (Inset: capacitive contribution ($|C_{cap}|$%) at j values of 5, 10, 20, 40, and 60 mV s^{-1}). (d) GCD profiles of S-30, S-50, and S-100 at $j = 1$ A g^{-1}. (e) GCD profile of S-50 at j values of 0.5, 1, 2, 4, 6, 8, 10, and 20 A g^{-1}. (f) Plot of specific capacitance (C_{sp}) at j values of 0.5, 1, 2, 4, 6, 8, 10, and 20 A g^{-1} for S-30, S-50, and S-100. (g) Plot of C_{sp} versus the number of cycles for $j = 8$ A g^{-1}. (Inset: plot of the first and last three cycles).

higher charging and discharging times compared with those of S-30 and S-100 at the same j value. This can be ascribed to the open porous structure of S-50, which facilitated the diffusion of ions, resulting in more faradic storage at the nanosheets. Fig. 4(e) shows the GCD curves of S-50 at j values of 0.5, 1, 2, 4, 6, 8, 10, and 20 A g^{-1}. All the GCD curves were symmetric, which implies the high columbic efficiency of the Mn-doped Co_3O_4 nanosheets [66]. Similar GCD behavior was observed for S-30 and S-100 at j values of 0.5, 1, 2, 4, 6, 8, 10, and 20 A g^{-1} (Figs. S3(c), (d)). The charge transfer rate at the electrode increased with increasing j, which rapidly changed the potential to effectively decrease the charge–discharge time. The capacitance (C) and specific capacitance (C_{sp}) can be calculated from the nonlinear GCD curves at different currents (I) using Eq. 6 and 7 as follows [67,68]:

$$C = \frac{2I\int V\Delta t}{(\Delta V)^2}(F) \tag{6}$$

$$C_{sp} = \frac{C}{m}\left(F{\cdot}g^{-1}\right) \tag{7}$$

where $\int V\Delta t$ is the area under the discharge curve, ΔV ($=E_f - E_i$) is the potential window limit, Δt is the discharge time, and m is the mass of the active electrode material.

The plots of the estimated C_{sp} versus j for S-30, S-50, and S-100 are shown in Fig. 4(f). Remarkably, S-50 exhibited the highest C_{sp} value for all the j values. A maximum C_{sp} of 1005 F g^{-1} is estimated for S-50 at 0.5 A g^{-1} in comparison to 581 F g^{-1} for S-30 and 351 F g^{-1} for S-100 at same j. The remarkable C_{sp} value obtained for S-50 can be ascribed to its mesoporous nanosheet-like morphology, which was tuned simply by changing the ν parameter of the CV during the electrochemical synthesis. This C_{sp} value is greater than that previously reported for Mn–Co-based metal oxide materials and nanomaterials synthesized by electrochemical methods (Table S1). The cyclic performance of S-50 was evaluated by performing 5000 GCD cycles at 8 A g^{-1}, as shown in Fig. 4 (g), the inset shows the first and final three GCD cycles. Initially, owing to the charging and discharging processes, numerous active sites developed at the porous nanosheets, increasing the C_{sp} value [66,69,70]. A superior cycling durability with 88% of its original capacitance retained after 5000 cycles at 8 A g^{-1} in electrolyte, which is much higher than previously reported electrodes' cycling durability (Table S2).

In further analysis, the EIS measurements were performed for S-30, S-50, and S-100 in the frequency (f) range of 0.1 Hz– 0.1 M Hz. The Nyquist plots representing the real (Z_{re}) and imaginary ($-Z_{img}$) components of the impedance which are depicted in Fig. 5(a). In addition, an equivalent circuit model was simulated for fitting the data to evaluate the surface electrochemical interaction of the nanostructured electrode. The associated simulated Nyquist and Bode plots (f-dependent impedance and phase) are shown in Fig. S4. The high-frequency region of impedance comprises a semicircle (inset in Fig. 5(a)), in which the intercept on Z_{re} represents the solution resistance (R_s) equivalent to the resistance associated with the contact among the conductor-active material, intrinsic resistance of the active material, and ionic resistance of the electrolyte. Here, S-30 exhibited R_s of 0.89 Ω which is higher than 0.84 Ω of S-50 and 0.85 Ω of S-100, indicating the porous structure of S-50 and S-100 generated more conductive pathway[71]. Moreover, the diameter of the semicircle represents the charge transfer resistance (R_{ct}). The impedance of the porous structure during redox transitions can be represented by R_{ct} [72]. The R_{ct} of S-30 was estimated to be 14.77 Ω, which was higher than 6.84 Ω of S-50 and 5.19 Ω of S-100 respectively. This indicates that the porous nanostructure exhibited low impedance in the charge transfer process. Fig. 5(b) shows the plot of log $|Z(\omega)|$ versus f, where $Z(\omega) = Z_{re}(\omega) + j\,Z_{img}(\omega)$, $\omega = 2\pi f$, and $j = -1^{1/2}$. The frequency-dependent impedance revealed the capacitive behavior of the electrode material. S-30 exhibited frequency-dependent impedance over a wide frequency range, which shows that the nanooctahedra structure of Mn-doped Co_3O_4 had more capacitive behavior owing to its compact nanostructure [73]. Fig. 5(c) shows a plot of the phase angle versus f, in which the capacitive frequency response of the electrode can be evaluated at a phase angle of $-45°$ ($f_{-45°}$). The $f_{-45°}$ obtained for S-30 is approximately 0.62 kHz which is higher than 14.3 Hz of S-50 and 15 Hz of S-100. This low-frequency response of the porous nanostructures demonstrates the pseudocapacitive behavior owing to the faradic charge storage occurring at the electrode pores [45]. Moreover, the capacitance ($C(\omega)$) behavior of the samples was studied by calculating the real ($C_{re}(\omega)$) and imaginary ($C_{img}(\omega)$) parts of the capacitance using Eqs. (8)–(10) [45,74]:

$$C(\omega) = C_{re}(\omega) - j\cdot C_{img}(\omega) \tag{8}$$

$$C_{re}(\omega) = \frac{-Z_{img}(\omega)}{\omega|Z(\omega)|^2} \tag{9}$$

$$C_{img}(\omega) = \frac{Z_{re}(\omega)}{\omega|Z(\omega)|^2} \tag{10}$$

where $C_{re}(\omega)$ is the actual accessible capacitance of the material, and $C_{img}(\omega)$ is the imaginary capacitance, which represents the energy dissipation of the material via an irreversible process. Fig. 5(d)–(f) show the plot of $C_{re}(\omega)/C_{img}(\omega)$ versus f. S-50 showed higher values of capacitance at low frequencies, demonstrating its higher power performance and excellent response rate. Then, the complex power $S(\omega)$ of the samples was examined according to Eq. 11 as follows [75]:

$$S(\omega) = P(\omega) + j\cdot Q(\omega) \tag{11}$$

where the active power $P(\omega)$ and reactive power $Q(\omega)$ can be expressed as

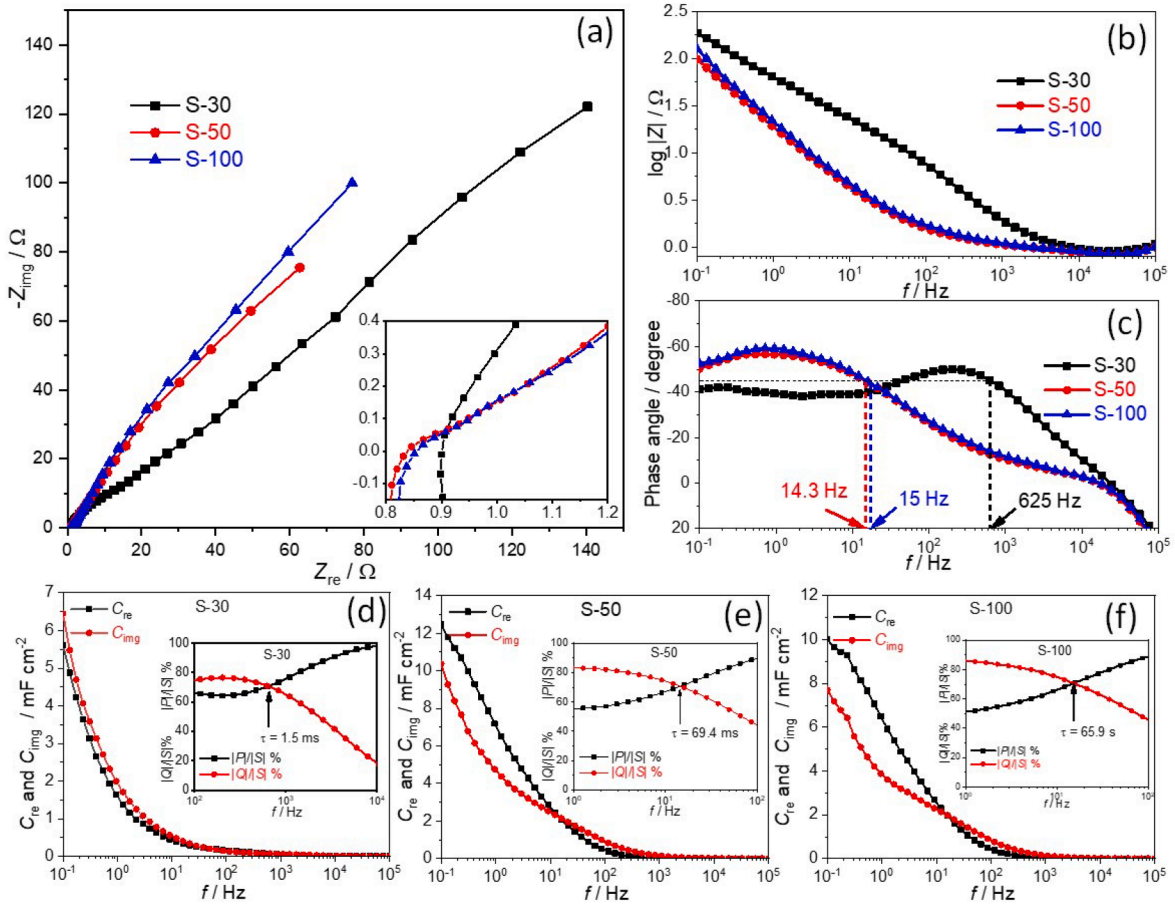

Fig. 5. (a) Nyquist plots of S-30, S-50, and S-100 (Inset: high-frequency region of the Nyquist plot). (b) Plot of log $|Z|$ versus f and (c) plot of phase angle versus f for S-30, S-50, and S-100. Plot of real capacitance (C_{re}) and imaginary capacitance (C_{img}) versus f for (d) S-30, (e) S-50, and (f) S-100. (Inset: plot of normalized active power $|P|/|S|$% and normalized reactive power $|Q|/|S|$% versus f).

$$P(\omega) = \omega C_{img}(\omega)\cdot|\Delta V_{rms}|^2 \quad (12)$$

$$Q(\omega) = -\omega C_{re}(\omega)\cdot|\Delta V_{rms}|^2 \quad (13)$$

Here, $|\Delta V_{\rm rms}|^2 = \Delta V_{\rm max}/\sqrt{2}$, where $\Delta V_{\rm max}$ is the maximum amplitude of the AC signal used for EIS. The complex power spectrum of the samples contained the plot of the normalized active power $|P(\omega)|/|S(\omega)|$ and normalized reactive power $|Q(\omega)|/|S(\omega)|$ versus f. The two plots crossed over at f_o, indicating the transition of the electrodes from capacitive to resistive behavior. The associated relaxation time ($\tau_o = 1/f_0$) represents the duration of energy discharge with more than 50% efficiency; it is also indicative of the discharge response of the electrode material. S-30 showed 1.5 ms of relaxation time, which is a smaller response time than 69.4 ms of S-50 and 65.9 ms of S-100. This suggests that most of the charges on S-30 were stored at the surface of the nanooctahedra, exhibiting its surface capacitive rather than intercalation diffusive behavior; similar to that observed in the case of S-50 and S-100. However, the value of 69.4 ms for S-50 is lower than that observed for carbon-based SC electrodes ($\tau_o = 6$ s) [76]. This EIS study confirms the CV behavior of the present samples.

To evaluate the performance of S-50 in an SC device, the aqueous electrode system was assembled using S-50 as a positive electrode and AC as a negative electrode in 2-M KOH. Fig. 6(a) and 6(b) show CV profiles and GCD profiles of an Mn-doped Co_3O_4//AC asymmetric SC within the potential limit of 1.6 V, respectively. All CV curves are nearly rectangular and the GCD curves are triangular, similarly to those of EDLC devices. This linear discharging behavior stems from the combined effect of AC as EDLC and the redox reactions occurring at the Mn-doped Co_3O_4 nanostructured electrode surface. The shape of the CV curves remained unaltered as the ν value increased, indicating excellent electrochemical reversibility of the asymmetric SC device. The assembled device also maintained excellent columbic efficiency at different j values. Fig. 6(c) shows the plot of the estimated $C_{\rm sp}$ of the device at different j values; the maximum $C_{\rm sp}$ of 53.80 F g^{-1} was obtained at 0.5 A g^{-1}. The specific energy (E) and specific power (P) of the assembled device were calculated by measuring the discharge time, as plotted in Ragone plot depicted in the inset in Fig. 6(c). The assembled device exhibited a maximum specific energy of 20.6 Wh kg^{-1} with a maximum specific power of 16 kW kg^{-1}, which is higher than that previously reported for Mn, Co-based oxides [6,36,77-79]. Furthermore, the cyclic stability of the asymmetric device assembly was tested during 2000 GCD cycles for $j = 3$ A g^{-1}. Fig. 6(d) shows the plot of capacity retention and coulombic efficiency as a function of the number of cycles. It was found that the assembled device retained 86% of the initial capacity after 2000 cycles, with a remarkable coulombic efficiency of 98%. Generally, dissolution of the active material in KOH can occur due to repeated charging and discharging cycles, which results in a deterioration in the device performance. However, the Mn-doped Co_3O_4 sample showed an excellent electrochemical performance, demonstrating its applicability in high-performance SC devices. This remarkable electrochemical performance can be ascribed to the combined pseudocapacitive charge storage at Mn and Co active sites and the mesoporous interconnected nanosheet assembly on the conductive porous Ni foam, which provides excellent electrical connectivity due to the binder-free formation of the active material via the electrochemical synthesis method.

4. Conclusion

A simple, binder-free electrochemical method was used to synthesize interconnected nanosheets of Mn-doped Co_3O_4 on Ni foam as a substrate. Formation of the nanostructures could be tuned by varying the CV conditions. Thus, at scan rates of 30, 50, and 100 mV s^{-1}, irregularly oriented nanooctahedra, interconnected standing nanosheets, and nanopetals, respectively, were formed on the Ni foam. A careful study showed that most of the electrochemical energy storage and retrieval varied strongly with the nanostructures. The standing interconnected nanosheets of Mn-doped Co_3O_4 exhibited remarkable SC performance with a maximum specific capacitance of 1005F g^{-1} and a superior cycling durability with 88% of its original capacitance after 5000 cycles

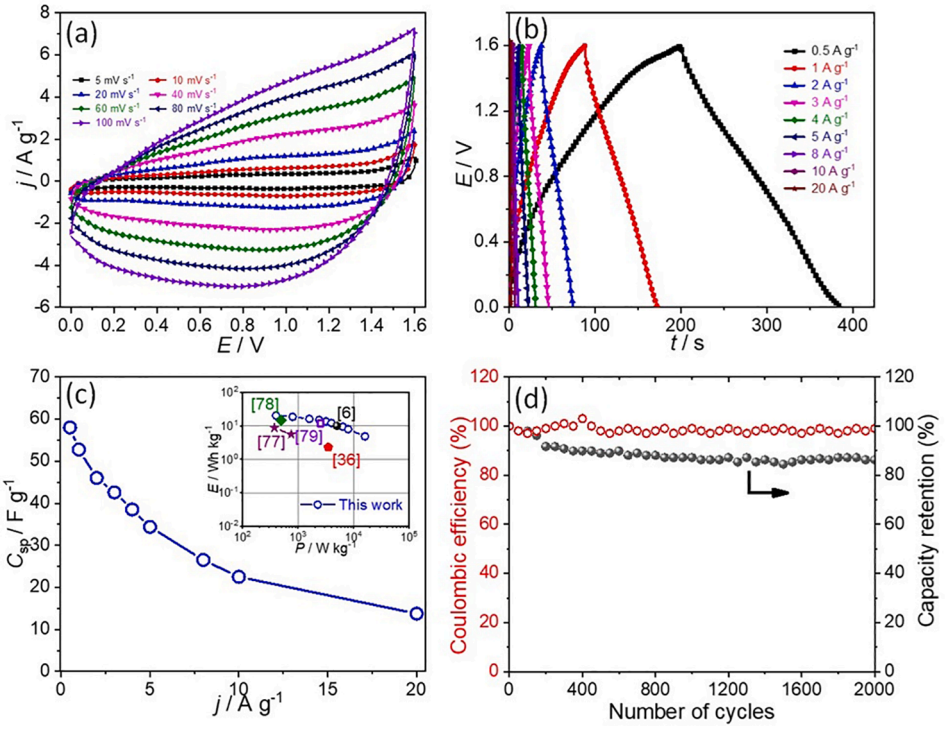

Fig. 6. (a) CV curves of the Mn-doped Co_3O_4//AC asymmetric SC device at scan rates (ν) values of 5, 10, 20, 40, 60, 80, and 100 mV s^{-1} within the potential limit of 1.6 V. (b) GCD curves of the device at current density (j) values of 0.5, 1, 2, 3, 4, 5, 8, 10, and 20 A g^{-1}. (c) Plot of $C_{\rm sp}$ versus j of the device at j values of 0.5, 1, 2, 3, 4, 5, 8, 10, and 20 A g^{-1}. (Inset: Ragone plot of the device). (d) Plot of coulombic efficiency and capacity retention of the device as a function of the number of cycles.

at 8 A g^{-1} in electrolyte. An asymmetric SC prepared by assembling the Mn-doped Co_3O_4 nanosheets with AC increased the potential of the device to 1.6 V and demonstrated a maximum specific energy of 20.6 Wh kg^{-1} and a maximum specific power of 16 kW kg^{-1} with 80.6% capacity retention after 2000 cycles. The interconnected nanosheets of Mn-doped Co_3O_4 exhibited low internal resistance and charge transfer resistance, which provided good electrical conductivity and additional active sites for faradic charge storage with minimum loss. This study highlights the importance of the design of optimal nanostructures for electrochemical energy storage.

Declaration of Competing Interest

The authors declare that they have no known competing financial interests or personal relationships that could have appeared to influence the work reported in this paper.

Acknowledgment

This research was supported by the Basic Science Research Program through the National Research Foundation of Korea (NRF) funded by the Ministry of Education (NRF-2018R1A6A1A03024962) and the Ministry of Science and ICT (NRF-2020R1A2C2100746).

Appendix A. Supplementary data

Supplementary data to this article can be found online at https://doi.org/10.1016/j.cej.2021.129767.

References

[1] V. Augustyn, P. Simon, B. Dunn, Pseudocapacitive oxide materials for high-rate electrochemical energy storage, Energy Environ. Sci. 7 (2014) 1597–1614.
[2] J. Jiang, Y. Li, J. Liu, X. Huang, C. Yuan, X.W.D. Lou, Recent advances in metal oxide-based electrode architecture design for electrochemical energy storage, Adv. Mater. 24 (2012) 5166–5180.
[3] M. Armand, J.-M. Tarascon, Building better batteries, Nature 451 (2008) 652–657.
[4] S.A. Ansari, N. Parveen, H.M. Kotb, A. Alshoaibi, Hydrothermally derived three-dimensional porous hollow double-walled Mn_2O_3 nanocubes as superior electrode materials for supercapacitor applications, Electrochim. Acta. 355 (2020), 136783.
[5] S.K. Meher, G.R. Rao, Ultralayered Co_3O_4 for high-performance supercapacitor applications, J. Phys. Chem. C. 115 (2011) 15646–15654.
[6] A.D. Jagadale, V.S. Kumbhar, R.N. Bulakhe, C.D. Lokhande, Influence of electrodeposition modes on the supercapacitive performance of Co_3O_4 electrodes, Energy. 64 (2014) 234–241.
[7] J. Xu, F. Huo, Y. Zhao, Y. Liu, Q. Yang, Y. Cheng, S. Min, Z. Jin, Z. Xiang, In-situ La doped Co_3O_4 as highly efficient photocatalyst for solar hydrogen generation, Int. J. Hydrogen Energy. 43 (2018) 8674–8682.
[8] L. Abdelhak, B. Amar, B. Bedhiaf, D. Cherifa, B. Hadj, Characterization of Mn-doped Co_3O_4 thin films prepared by sol gel-based dip-coating process, High Temp. Mater. Process. 38 (2019) 237–247.
[9] H. Chen, J. Wang, F. Liao, X. Han, C. Xu, Y. Zhang, Facile synthesis of porous Mn-doped Co_3O_4 oblique prisms as an electrode material with remarkable pseudocapacitance, Ceram. Int. 45 (2019) 8008–8016.
[10] C. Stella, N. Soundararajan, K. Ramachandran, Structural, optical, and magnetic properties of Mn and Fe-doped Co_3O_4 nanoparticles, AIP Adv. 5 (2015) 087104.
[11] X.-Z. Liu, T. Tang, W.-J. Jiang, Q.-H. Zhang, L. Gu, J.-S. Hu, Fe-doped Co_3O_4 polycrystalline nanosheets as a binder-free bifunctional cathode for robust and efficient zinc–air batteries, Chem. Commun. 56 (2020) 5374–5377.
[12] T. Grewe, X. Deng, H. Tüysüz, Influence of Fe doping on structure and water oxidation activity of nanocast Co_3O_4, Chem. Mater. 26 (2014) 3162–3168.
[13] C. Xiao, X. Lu, C. Zhao, Unusual synergistic effects upon incorporation of Fe and/or Ni into mesoporous Co_3O_4 for enhanced oxygen evolution, Chem. Commun. 50 (2014) 10122–10125.
[14] H. Mahmoudi-Moghaddam, S. Tajik, H. Beitollahi, Highly sensitive electrochemical sensor based on La^{3+}-doped Co_3O_4 nanocubes for determination of sudan I content in food samples, Food Chem. 286 (2019) 191–196.
[15] S. Tajik, H. Mahmoudi-Moghaddam, H. Beitollahi, Screen-printed electrode modified with La^{3+}-doped Co_3O_4 nanocubes for electrochemical determination of hydroxylamine, J. Electrochem. Soc. 166 (2019) B402–B406.
[16] H. Beitollahi, H. Mahmoudi-Moghaddam, S. Tajik, S. Jahani, A modified screen printed electrode based on La^{3+}-doped Co_3O_4 nanocubes for determination of sulfite in real samples, Microchem. J. 147 (2019) 590–597.
[17] X. Zou, J. Su, R. Silva, A. Goswami, B.R. Sathe, T. Asefa, Efficient oxygen evolution reaction catalyzed by low-density Ni-doped Co_3O_4 nanomaterials derived from metal-embedded graphitic C_3N_4, Chem. Commun. 49 (2013) 7522–7524.
[18] X. Tong, X. Xia, C. Guo, Y. Zhang, J. Tu, H.J. Fan, X.-Y. Guo, Efficient oxygen reduction reaction using mesoporous Ni-doped Co_3O_4 nanowire array electrocatalysts, J. Mater. Chem. A. 3 (2015) 18372–18379.
[19] Z. Ren, Z. Wu, W. Song, W. Xiao, Y. Guo, J. Ding, S.L. Suib, P.-X. Gao, Low temperature propane oxidation over Co_3O_4 based nano-array catalysts: Ni dopant effect, reaction mechanism and structural stability, Appl. Catal. B Environ. 180 (2016) 150–160.
[20] J. Luo, Y. Wang, F. Wang, F. Li, L. Li, N. Zhao, F. Xiao, Aerobic oxidation of fluorene to fluorenone over copper-doped Co_3O_4 with a high specific surface area, ACS Sustain. Chem. Eng. 8 (2020) 2568–2576.
[21] T. Baidya, T. Murayama, P. Bera, O.V. Safonova, P. Steiger, N.K. Katiyar, K. Biswas, M. Haruta, Low-temperature CO oxidation over combustion made Fe- and Cr-doped Co_3O_4 catalysts: role of dopant's nature toward achieving sperior catalytic activity and stability, J. Phys. Chem. C. 121 (2017) 15256–15265.
[22] Y. Li, X. Ma, S. Guo, B. Wang, D. Sun, X. Zhang, S. Ruan, Hydrothermal synthesis and enhanced xylene-sensing properties of pompon-like Cr-doped Co_3O_4 hierarchical nanostructures, RSC Adv. 6 (2016) 22889–22895.
[23] K. Lu, T. Gu, L. Zhang, Z. Wu, R. Wang, X. Li, POM-assisted coating of MOF-derived Mo-doped Co_3O_4 nanoparticles on carbon nanotubes for upgrading oxygen evolution reaction, Chem. Eng. J. 127352 (2020).
[24] K. Cheng, F. Yang, Y. Xu, L. Cheng, Y. Bao, D. Cao, G. Wang, Pd doped Co_3O_4 nanowire array as the H_2O_2 electroreduction catalyst, J. Power Sources. 240 (2013) 442–447.
[25] S. Deng, X. Xiao, G. Chen, L. Wang, Y. Wang, Cd doped porous Co_3O_4 nanosheets as electrode material for high performance supercapacitor application, Electrochim. Acta. 196 (2016) 316–327.
[26] M. Chowdhury, F. Cummings, M. Kebede, V. Fester, Binderless solution processed Zn doped Co_3O_4 film on FTO for rapid and selective non-enzymatic glucose detection, Electroanalysis 29 (2017) 578–586.
[27] H. Hu, S. Cai, H. Li, L. Huang, L. Shi, D. Zhang, In Situ DRIFTs Investigation of the low-temperature reaction mechanism over Mn-doped Co_3O_4 for the selective catalytic Reduction of NO_x with NH_3, J. Phys. Chem. C. 119 (2015) 22924–22933.
[28] G. Li, M. Chen, Y. Ouyang, D. Yao, L. Lu, L. Wang, X. Xia, W. Lei, S.-M. Chen, D. Mandler, Q. Hao, Manganese doped Co_3O_4 mesoporous nanoneedle array for long cycle-stable supercapacitors, Appl. Surf. Sci. 469 (2019) 941–950.
[29] C. Liu, L. Gong, R. Dai, M. Lu, T. Sun, Q. Liu, X. Huang, Z. Huang, Mesoporous Mn promoted Co_3O_4 oxides as an efficient and stable catalyst for low temperature oxidation of CO, Solid State Sci. 71 (2017) 69–74.
[30] Y. Ma, M. Zha, Y. Dong, L. Li, G. Hu, Mn-doped Co_3O_4 nanoarrays as a promising electrocatalyst for oxygen evolution reaction, Mater. Res. Express. 6 (2019), 115033.
[31] R.S. Kalubarme, S.M. Jadhav, B.B. Kale, S.W. Gosavi, C. Terashima, A. Fujishima, Porous Mn-doped cobalt oxide@C nanocomposite: A stable anode material for Li-ion rechargeable batteries, Nanotechnology. 29 (2018).
[32] M. Kalyani, R.N. Emerson, Electrochemical performance of Mn doped Co_3O_4 thin film electrodes by electrodeposition method, Int. J. Res. Appl. Sci. Eng. Technol. 7 (2019) 76–86.
[33] H. Chen, J. Wang, F. Liao, X. Han, Y. Zhang, C. Xu, L. Gao, Uniform and porous Mn-doped Co_3O_4 microspheres: Solvothermal synthesis and their superior supercapacitor performances, Ceram. Int. 45 (2019) 11876–11882.
[34] H. Chen, J. Wang, F. Liao, X. Han, C. Xu, Y. Zhang, Facile synthesis of porous Mn-doped Co_3O_4 oblique prisms as an electrode material with remarkable pseudocapacitance, Ceram. Int. 45 (2019) 8008–8016.
[35] S.A. Ansari, N.A. Khan, Z. Hasan, A.A. Shaikh, F.K. Ferdousi, H.R. Barai, N.S. Lopa, M.M. Rahman, Electrochemical synthesis of titanium nitride nanoparticles onto titanium foil for electrochemical supercapacitors with ultrafast charge/discharge, Sustain. Energy Fuels 4 (2020) 2480–2490.
[36] S. Sahoo, K.K. Naik, C.S. Rout, Electrodeposition of spinel $MnCo_2O_4$ nanosheets for supercapacitor applications, Nanotechnology 26 (2015) 455401.
[37] G.W. Yang, C.L. Xu, H.L. Li, Electrodeposited nickel hydroxide on nickel foam with ultrahigh capacitance, Chem. Commun. 48 (2008) 6537–6539.
[38] A. Roy, H.S. Jadhav, G.M. Thorat, J.G. Seo, Electrochemical growth of $Co(OH)_2$ nanoflakes on Ni foam for methanol electro-oxidation, New J. Chem. 41 (2017) 9546–9553.
[39] N.R. Chodankar, D.P. Dubal, S.-H. Ji, D.-H. Kim, Superfast electrodeposition of newly developed $RuCo_2O_4$ nanobelts over low-cost stainless steel mesh for high-performance aqueous supercapacitor, Adv. Mater. Interfaces 5 (2018) 1800283.
[40] N.C. Maile, S.K. Shinde, R.T. Patil, A.V. Fulari, R.R. Koli, D.-Y. Kim, D.S. Lee, V. J. Fulari, Structural and morphological changes in binder-free $MnCo_2O_4$ electrodes for supercapacitor applications: effect of deposition parameters, J. Mater. Sci. Mater. Electron. 30 (2019) 3729–3743.
[41] N.C. Maile, S.K. Shinde, S.S. Patil, D.Y. Kim, A.V. Fulari, D.S. Lee, V.J. Fulari, Capacitive property studies of electrochemically synthesized Co_3O_4 and Mn_3O_4 on inexpensive stainless steel current collector for supercapacitor application, Ceram. Int. 46 (2020) 14640–14649.
[42] J. Yang, E. Zhang, X. Li, Y. Yu, J. Qu, Z.Z. Yu, Direct reduction of graphene oxide by Ni foam as a high-capacitance supercapacitor electrode, ACS Appl. Mater. Interfaces 8 (2016) 2297–2305.
[43] M. Fang, G. Dong, R. Wei, J.C. Ho, Hierarchical nanostructures: Design for sustainable water splitting, Adv. Energy Mater. 7 (2017) 1–25.
[44] D.A. Aikens, Electrochemical methods, fundamentals and applications, J. Chem. Educ. 60 (1983) A25.
[45] D.P. Dubal, N.R. Chodankar, R. Holze, D.H. Kim, P. Gomez-Romero, Ultrathin mesoporous $RuCo_2O_4$ nanoflakes: an advanced electrode for high-performance asymmetric supercapacitors, ChemSusChem 10 (2017) 1771–1782.

[46] W. Zhu, X. Yue, W. Zhang, S. Yu, Y. Zhang, J. Wang, J. Wang, Nickel sulfide microsphere film on Ni foam as an efficient bifunctional electrocatalyst for overall water splitting, Chem. Commun. 52 (2016) 1486–1489.
[47] Z. Chen, C.X. Kronawitter, B.E. Koel, Facet-dependent activity and stability of Co_3O_4 nanocrystals towards the oxygen evolution reaction, Phys. Chem. Chem. Phys. 17 (2015) 29387–29393.
[48] B. Saravanakumar, G. Ravi, V. Ganesh, R.K. Guduru, R. Yuvakkumar, $MnCo_2O_4$ nanosphere synthesis for electrochemical applications, Mater. Sci. Energy Technol. 2 (2019) 130–138.
[49] V.G. Hadjiev, M.N. Iliev, I.V. Vergilov, The Raman spectra of Co_3O_4, J. Phys. C Solid State Phys. 21 (1988) L199–L201.
[50] S. Mo, S. Li, Q. Ren, M. Zhang, Y. Sun, B. Wang, Z. Feng, Q. Zhang, Y. Chen, D. Ye, Vertically-aligned Co_3O_4 arrays on Ni foam as monolithic structured catalysts for CO oxidation: effects of morphological transformation, Nanoscale. 10 (2018) 7746–7758.
[51] P.L. Meena, S. Pal, K. Sreenivas, R.A. Kumar, Structural and magnetic properties of $MnCo_2O_4$ spinel multiferroic, Adv. Sci. Lett. 21 (2015) 2760–2763.
[52] V. Venkatachalam, A. Alsalme, A. Alghamdi, R. Jayavel, High performance electrochemical capacitor based on $MnCo_2O_4$ nanostructured electrode, J. Electroanal. Chem. 756 (2015) 94–100.
[53] L. Kuang, F. Ji, X. Pan, D. Wang, X. Chen, D. Jiang, Y. Zhang, B. Ding, Mesoporous $MnCo_2O_{4.5}$ nanoneedle arrays electrode for high-performance asymmetric supercapacitor application, Chem. Eng. J. 315 (2017) 491–499.
[54] N. Parveen, Z. Khan, S.A. Ansari, S. Park, S.T. Senthilkumar, Y. Kim, H. Ko, M. H. Cho, Feasibility of using hollow double walled Mn_2O_3 nanocubes for hybrid Na-air battery, Chem. Eng. J. 360 (2019) 415–422.
[55] X. Li, X.H. Niu, H.Y. Wu, S.C. Meng, W.C. Zhang, J.M. Pan, F.X. Qiu, Impedimetric enzyme-free detection of glucose via a computation-designed molecularly imprinted electrochemical sensor fabricated on porous Ni foam, Electroanalysis 29 (2017) 1243–1251.
[56] Q. Wang, L. Jiao, H. Du, J. Yang, Q. Huan, W. Peng, Y. Si, Y. Wang, H. Yuan, Facile synthesis and superior supercapacitor performances of three-dimensional cobalt sulfide hierarchitectures, CrystEngComm 13 (2011) 6960–6963.
[57] Y. Xu, X. Wang, C. An, Y. Wang, L. Jiao, H. Yuan, Facile synthesis route of porous $MnCo_2O_4$ and $CoMn_2O_4$ nanowires and their excellent electrochemical properties in supercapacitors, J. Mater. Chem. A. 2 (2014) 16480–16488.
[58] Y. Fu, H. He, X. Li, L. Wu, R. Yan, J. Zhang, X. Xu, F. Wang, Enhance supercapacitive performance of Ni foam electrode and $MnCo_2O_{4.5}$/Ni foam electrode, J. Mater. Sci. Mater. Electron. 28 (2017) 1562–1571.
[59] A. Krittayavathananon, T. Pettong, P. Kidkhunthod, M. Sawangphruk, Insight into the charge storage mechanism and capacity retention fading of $MnCo_2O_4$ used as supercapacitor electrodes, Electrochim. Acta. 258 (2017) 1008–1015.
[60] Y. Dong, Y. Wang, Y. Xu, C. Chen, Y. Wang, L. Jiao, H. Yuan, Facile synthesis of hierarchical nanocage $MnCo_2O_4$ for high performance supercapacitor, Electrochim. Acta. 225 (2017) 39–46.
[61] R.R. Salunkhe, J. Tang, Y. Kamachi, T. Nakato, J.H. Kim, Y. Yamauchi, Asymmetric supercapacitors using 3D nanoporous carbon and cobalt oxide electrodes synthesized from a single metal–organic framework, ACS Nano. 9 (2015) 6288–6296.
[62] J. Xu, Y. Sun, M. Lu, L. Wang, J. Zhang, E. Tao, J. Qian, X. Liu, Fabrication of the porous $MnCo_2O_4$ nanorod arrays on Ni foam as an advanced electrode for asymmetric supercapacitors, Acta Mater. 152 (2018) 162–174.
[63] X. Dong, X. Wang, L. Wang, H. Song, H. Zhang, W. Huang, P. Chen, 3D Graphene foam as a monolithic and macroporous carbon electrode for electrochemical sensing, ACS Appl. Mater. Interfaces 4 (2012) 3129–3133.
[64] J. Liu, J. Wang, C. Xu, H. Jiang, C. Li, L. Zhang, J. Lin, Z.X. Shen, Advanced energy storage devices:basic principles, analytical methods, and rational materials design, Adv. Sci. 5 (2018) 1700322.
[65] N. Zhao, H. Fan, J. Ma, M. Zhang, C. Wang, H. Li, X. Jiang, X. Cao, Entire synergistic contribution of electrodeposited battery-type $NiCo_2O_4$@$Ni_{4.5}Co_{4.5}S_8$ composite for high-performance supercapacitors, J. Power Sources 439 (2019), 227097.
[66] C. Yuan, J. Li, L. Hou, X. Zhang, L. Shen, X.W. Lou, Ultrathin mesoporous $NiCo_2O_4$ nanosheets supported on Ni foam as advanced electrodes for supercapacitors, Adv. Funct. Mater. 22 (2012) 4592–4597.
[67] N.C. Maile, S.K. Shinde, R.R. Koli, A.V. Fulari, D.Y. Kim, V.J. Fulari, Effect of different electrolytes and deposition time on the supercapacitor properties of nanoflake-like $Co(OH)_2$ electrodes, Ultrason, Sonochem 51 (2019) 49–57.
[68] R.B. Waghmode, N.C. Maile, D.S. Lee, A.P. Torane, Chemical bath synthesis of $NiCo_2O_4$ nanoflowers with nanorods like thin film for flexible supercapacitor application-effect of urea concentration on structural conversion, Electrochim. Acta. 350 (2020), 136413.
[69] X. Guo, M. Li, Y. Liu, Y. Huang, S. Geng, W. Yang, Y. Yu, Hierarchical core-shell electrode with $NiWO_4$ nanoparticles wrapped $MnCo_2O_4$ nanowire arrays on Ni foam for high-performance asymmetric supercapacitors, J. Colloid Interface Sci. 563 (2020) 405–413.
[70] S.G. Krishnan, M.H.A. Rahim, R. Jose, Synthesis and characterization of $MnCo_2O_4$cuboidal microcrystals as a high performance psuedocapacitor electrode, J. Alloy. Compd. 656 (2016) 707–713.
[71] L. Bin Kong, C. Lu, M.C. Liu, Y.C. Luo, L. Kang, X. Li, F.C. Walsh, The specific capacitance of sol-gel synthesised spinel $MnCo_2O_4$ in an alkaline electrolyte, Electrochim. Acta 115 (2014) 22–27.
[72] G.K. Mishra, R. Kant, Modular theory for DC-biased electrochemical impedance response of supercapacitor, J. Power Sources 473 (2020), 228467.
[73] C.C. Hu, W.C. Chen, Effects of substrates on the capacitive performance of $RuO_x{\cdot}nH_2O$ and activated carbon-RuO_x electrodes for supercapacitors, Electrochim. Acta 49 (2004) 3469–3477.
[74] C. Portet, P.L. Taberna, P. Simon, E. Flahaut, Influence of carbon nanotubes addition on carbon-carbon supercapacitor performances in organic electrolyte, J. Power Sources 139 (2005) 371–378.
[75] D. Jain, J. Kanungo, S.K. Tripathi, Synergistic approach with redox additive for the development of environment benign hybrid supercapacitor, J. Electrochem. Soc. 166 (2019) A3168–A3181.
[76] A. Adan-Mas, L. Alcaraz, P. Arévalo-Cid, F.A. López-Gómez, F. Montemor, Coffee-derived activated carbon from second biowaste for supercapacitor applications, Waste Manag. 120 (2021) 280–289.
[77] E. Dai, J. Xu, J. Qiu, S. Liu, P. Chen, Y. Liu, Co@Carbon and Co_3O_4@Carbon nanocomposites derived from a single MOF for supercapacitors, Sci. Rep. 7 (2017) 12588.
[78] M. Shanmugavadivel, V.V. Dhayabaran, M. Subramanian, Fabrication of high energy and high power density supercapacitor based on $MnCo_2O_4$ nanomaterial, J. Phys. Chem. Solids 133 (2019) 15–20.
[79] R.R. Salunkhe, B.P. Bastakoti, C.-T. Hsu, N. Suzuki, J.H. Kim, S.X. Dou, C.-C. Hu, Y. Yamauchi, Direct growth of cobalt hydroxide rods on nickel foam and its application for energy storage, Chem. - A Eur. J. 20 (2014) 3084–3088.